Two types of axisymmetric helical magnetorotational instability in rotating flows with positive shear

George Mamatsashvili [*]

*Niels Bohr International Academy, Niels Bohr Institute, Blegdamsvej 17, 2100 Copenhagen, Denmark
and Helmholtz-Zentrum Dresden-Rossendorf, Bautzner Landstraße 400, D-01328 Dresden, Germany*

Frank Stefani

Helmholtz-Zentrum Dresden-Rossendorf, Bautzner Landstraße 400, D-01328 Dresden, Germany

Rainer Hollerbach

Department of Applied Mathematics, University of Leeds, Leeds LS2 9JT, United Kingdom

Günther Rüdiger

Leibniz-Institut für Astrophysik Potsdam, An der Sternwarte 16, D-14482 Potsdam, Germany

We reveal and investigate a type of linear axisymmetric helical magnetorotational instability which is capable of destabilizing viscous and resistive rotational flows with radially increasing angular velocity, or positive shear. This instability is double-diffusive by nature and is different from the more familiar helical magnetorotational instability, operating at positive shear above the Liu limit, in that it works instead for a wide range of the positive shear when (i) a combination of axial and azimuthal magnetic fields is applied and (ii) the magnetic Prandtl number is not too close to unity. We study this instability first with radially local Wentzel-Kramers-Brillouin (WKB) analysis, deriving the scaling properties of its growth rate with respect to Hartmann, Reynolds, and magnetic Prandtl numbers. Then we confirm its existence using a global stability analysis of the magnetized flow confined between two rotating coaxial cylinders with purely conducting or insulating boundaries and compare the results with those of the local analysis. From an experimental point of view, we also demonstrate the presence of this instability in a magnetized viscous and resistive Taylor-Couette flow with positive shear for such values of the flow parameters, which can be realized in upcoming experiments at the DRESDYN facility. Finally, this instability might have implications for the dynamics of the equatorial parts of the solar tachocline and dynamo action there, since the above two necessary conditions for the instability to take place are satisfied in this region. Our global stability calculations for the tachocline-like configuration, representing a thin rotating cylindrical layer with the appropriate boundary conditions—conducting inner and insulating outer cylinders—and the values of the flow parameters, indicate that it can indeed arise in this case with a characteristic growth time comparable to the solar cycle period.

---

[*]george.mamatsashvili@nbi.ku.dk

I. INTRODUCTION

According to Rayleigh's criterion [1], rotating flows of ideal fluids with radially increasing specific angular momentum are linearly stable. This result has severe astrophysical consequences, implying hydrodynamic stability of Keplerian rotation in accretion disks. Nowadays, the magnetorotational instability (MRI) [2–4] is considered to be the most likely destabilizing mechanism for these disks, driving radially outward transport of angular momentum and inward accretion of mass.

The standard MRI (SMRI, with a purely axial magnetic field, [2–4]), as well as the nonaxisymmetric azimuthal MRI (AMRI, with a purely azimuthal magnetic field, [5]) and the axisymmetric helical MRI (HMRI, with combined axial and azimuthal magnetic fields, [6]) have all been extensively studied theoretically (see a recent review [7] and references therein). The inductionless forms of AMRI and HMRI have also been obtained in liquid metal experiments [8–10], while unambiguous experimental evidence for inductive SMRI remains elusive, despite promising first results [11,12].

In contrast to Keplerian-like rotation with increasing angular momentum but decreasing angular velocity, much less attention is usually devoted to flows with increasing angular velocity. Until recently, such flows have been believed to be strongly stable, even under magnetic fields. However, for very high Reynolds numbers, $\text{Re} \sim 10^7$, they can yield nonaxisymmetric linear instability [13]. Apart from this hydrodynamic instability, there is also a special type of AMRI operating in flows with much lower Reynolds number but sufficiently strong positive shear [14–16]. This restriction to strong shear makes, however, this so-called *Super-AMRI* astrophysically less significant. One of few positive shear regions is a portion of the solar tachocline extending $\pm 30°$ about the Sun's equator. Even there, the shear measured in terms of Rossby number $\text{Ro} = r(2\Omega)^{-1} d\Omega/dr$ is only around 0.7 [17,18], much less than the so-called *upper Liu limit* (ULL) $\text{Ro}_{ULL} = 2(1 + \sqrt{2}) \approx 4.83$ [19] required for Super-AMRI. Another astrophysical system in which positive shear is expected is the boundary layer between an accretion disk and its host star [20,21].

Given a general similarity between AMRI and HMRI and the universal nature of the Liu limits [22,23], one might expect a similar result to hold also for *Super-HMRI*. However, as we report in this paper, there exists another type of axisymmetric HMRI, which we refer to as type 2 Super-HMRI, that operates in positive shear flows with arbitrary steepness, whereas the more familiar HMRI operating only at high enough positive shear above the Liu limit, $\text{Ro} > \text{Ro}_{ULL}$, is labeled type 1 Super-HMRI. The only requirements are (i) the presence of both axial and azimuthal magnetic field components and (ii) that the magnetic Prandtl number is neither zero (the inductionless limit) nor too close to unity. These conditions are indeed satisfied in the solar tachocline, where this instability can possibly play an important role in its dynamics and magnetic activity. Although this requires a detailed separate study and is out of the scope of the present paper, we have also done calculations at the end of this paper showing the possibility of occurrence of this instability for the tachocline-like configuration and parameters, but still remaining in the framework of cylindrical flow. The resulting growth time (inverse of the exponential growth rate) of the most unstable mode in fact turns out to be comparable to the solar cycle period.

In this paper, we carry out a linear stability analysis of a magnetic rotational flow in cylindrical geometry mainly using the Wentzel-Kramers-Brillouin (WKB) short-wavelength formulation of the underlying magnetohydrodynamics (MHD) problem [23,24], which is especially useful for understanding the basic features and scaling properties of this instability. This local analysis is then complemented by global, radially one-dimensional (1D) calculations of the corresponding unstable eigenmodes with the primary aim of demonstrating the existence of this version of Super-HMRI beyond the local WKB approximation as well as to draw a comparison with the results obtained using this approximation. A more comprehensive global linear analysis exploring parameter space and subsequently nonlinear analysis of this double-diffusive type 2 Super-HMRI at positive shear will be presented elsewhere.

The paper is organized as follows. The main equations and the formulation of a problem are given in Sec. II. The local WKB analysis of the instability is presented in Sec. III. The global stability

analysis of a differentially rotating flow between two coaxial cylinders at positive shear both in the narrow and wide gap cases as well as a comparison with the results of the local analysis are presented in Sec. IV. A summary and discussion on the relevance of this new version of Super-HMRI to the solar tachocline are given in Sec. V.

II. MAIN EQUATIONS

The motion of an incompressible conducting medium with constant viscosity ν and Ohmic resistivity η is governed by the equations of nonideal MHD

$$\frac{\partial \mathbf{U}}{\partial t} + (\mathbf{U} \cdot \nabla)\mathbf{U} = -\frac{1}{\rho}\nabla\left(P + \frac{\mathbf{B}^2}{2\mu_0}\right) + \frac{(\mathbf{B} \cdot \nabla)\mathbf{B}}{\mu_0\rho} + \nu\nabla^2\mathbf{U}, \tag{1}$$

$$\frac{\partial \mathbf{B}}{\partial t} = \nabla \times (\mathbf{U} \times \mathbf{B}) + \eta\nabla^2\mathbf{B}, \tag{2}$$

$$\nabla \cdot \mathbf{U} = 0, \quad \nabla \cdot \mathbf{B} = 0, \tag{3}$$

where ρ is the constant density, $\mathbf{U}$ is the velocity, P is the thermal pressure, $\mathbf{B}$ is the magnetic field, and μ_0 is the magnetic permeability of vacuum.

Consider a flow between two coaxial cylinders at inner, r_i, and outer, r_o, radii, rotating, respectively, with angular velocities Ω_i and Ω_o in the cylindrical coordinates (r, ϕ, z). Since we are primarily interested in the flow stability in the case of positive shear, or so-called super-rotation [15,16], the inner cylinder is assumed to rotate more slowly than the outer one, $\Omega_i < \Omega_o$, inducing an azimuthal nonuniform flow $\mathbf{U}_0 = [0, r\Omega(r), 0]$ between the cylinders with radially increasing angular velocity, $d\Omega/dr > 0$, and hence positive Rossby number, Ro > 0. The pressure associated with this base flow and maintaining its rotation is denoted as P_0. The imposed background helical magnetic field $\mathbf{B}_0 = [0, B_{0\phi}(r), B_{0z}]$ consists of a radially varying, current-free azimuthal component, $B_{0\phi}(r) = \beta B_{0z}r_o/r$, and a constant axial component, B_{0z}, where the constant parameter β characterizes field's helicity.

We investigate the linear stability of this equilibrium against small *axisymmetric* $(\partial/\partial\phi = 0)$ perturbations, $\mathbf{u} = \mathbf{U} - \mathbf{U}_0$, $p = P - P_0$, and $\mathbf{b} = \mathbf{B} - \mathbf{B}_0$, which are all functions of r and depend on time t and axial-vertical z coordinate via $\propto\exp(\gamma t + ik_z z)$, where γ is the (complex) eigenvalue and k_z is the axial wave number. There is instability in the flow, if the real part (growth rate) of any eigenvalue is positive, Re$(\gamma) > 0$. In such cases, for a given set of parameters, we always select out the mode with the largest growth rate from a corresponding eigenvalue spectrum.

III. WKB ANALYSIS

In this section, we use a radially local WKB approximation, where the radial dependence of the perturbations is assumed to be of the form $\propto\exp(ik_r r)$ with k_r being the radial wave number. The resulting dispersion relation, which follows from Eqs. (1)–(3) after linearizing and substituting the above exponential form of the perturbations, is represented by the fourth-order polynomial [23,24]:

$$\gamma^4 + a_1\gamma^3 + a_2\gamma^2 + (a_3 + ib_3)\gamma + a_4 + ib_4 = 0, \tag{4}$$

with the real coefficients

$$a_1 = 2\frac{k^2}{\text{Re}}\left(1 + \frac{1}{\text{Pm}}\right),$$

$$a_2 = 4\alpha^2(1 + \text{Ro}) + 2\left(k_z^2 + 2\alpha^2\beta^2\right)\frac{\text{Ha}^2}{\text{Re}^2\text{Pm}} + \frac{k^4}{\text{Re}^2}\left(1 + \frac{4}{\text{Pm}} + \frac{1}{\text{Pm}^2}\right),$$

$$a_3 = 8(1 + \text{Ro})\alpha^2 \frac{k^2}{\text{RePm}} + 2\big[k^4 + (k_z^2 + 2\alpha^2\beta^2)\text{Ha}^2\big]\frac{k^2}{\text{Re}^3\text{Pm}}\left(1 + \frac{1}{\text{Pm}}\right),$$

$$b_3 = -8\alpha^2\beta k_z \frac{\text{Ha}^2}{\text{Re}^2\text{Pm}},$$

$$a_4 = 4\alpha^2 \frac{k^4}{\text{Pm}^2}\left[(1 + \text{Ro})\frac{1}{\text{Re}^2} + \beta^2\frac{\text{Ha}^2}{\text{Re}^4}\right] + 4\alpha^2 k_z^2 \text{Ro}\frac{\text{Ha}^2}{\text{Re}^2\text{Pm}} + \big(k_z^2\text{Ha}^2 + k^4\big)^2\frac{1}{\text{Re}^4\text{Pm}^2},$$

$$b_4 = 4\beta k_z^3\left[\text{Ro}\left(1 - \frac{1}{\text{Pm}}\right) - \frac{2}{\text{Pm}}\right]\frac{\text{Ha}^2}{\text{Re}^3\text{Pm}}.$$

Henceforth, γ is normalized by the outer cylinder's angular velocity Ω_o and the wave numbers by its inverse radius, r_o^{-1}. Other nondimensional parameters are $\alpha = k_z/k$, where $k = (k_r^2 + k_z^2)^{1/2}$ is the total wave number; the Reynolds number $\text{Re} = \Omega_o r_o^2/\nu$; the magnetic Reynolds number $\text{Rm} = \Omega_o r_o^2/\eta$, and their ratio, the magnetic Prandtl number $\text{Pm} = \nu/\eta = \text{Rm}/\text{Re}$; and the Hartmann number $\text{Ha} = B_{0z}r_o/(\mu_0\rho\nu\eta)^{1/2}$ that measures the strength of the imposed axial magnetic field. Another quantity characterizing the field is Lundquist number $S = \text{HaPm}^{1/2}$, which, like Rm, does not involve viscosity. Since we focus on positive Rossby numbers, $\text{Ro} > 0$, or positive shear, the flow is generally stable both hydrodynamically, according to Rayleigh's criterion (but see Ref. [13]), as well as against SMRI with a purely axial field ($\beta = 0$) [24–26].

In the inductionless limit, $\text{Pm} \to 0$, the roots of Eq. (4) can be found analytically [19,23,24,27,28]. For positive and relatively large $\text{Ro} > \text{Ro}_{ULL}$, one of the roots always has a positive real part, implying instability with the growth rate

$$\text{Re}(\gamma) = \sqrt{2X + 2\sqrt{X^2 + Y^2}} - \big(k_z^2 + 2\alpha^2\beta^2\big)\frac{\text{Ha}^2}{k^2\text{Re}} - \frac{k^2}{\text{Re}}, \tag{5}$$

where

$$X = \alpha^2\beta^2\big(\alpha^2\beta^2 + k_z^2\big)\frac{\text{Ha}^4}{\text{Re}^2 k^4} - \alpha^2(1 + \text{Ro}), \quad Y = \beta\alpha^2 k_z(2 + \text{Ro})\frac{\text{Ha}^2}{k^2\text{Re}},$$

which we call type 1 Super-HMRI. Our main goal, though, is to reveal that apart from this type 1 Super-HMRI at large positive shear, Eq. (4) also yields a different type of dissipation-induced double-diffusive instability at finite Pm, which we call type 2 Super-HMRI.

Regarding the dependence on β parameter in Eqs. (4) and (5), it is readily seen that, as long as $\beta \neq 0$, it enters the coefficients of these dispersion relations through the rescaled wave numbers, Hartmann, Lundquist, and Reynolds numbers, $k_z^* \equiv k_z/\beta$, $k^* \equiv k/\beta$, $\text{Ha}^* \equiv Ha/\beta$, $S^* \equiv S/\beta$, $\text{Re}^* \equiv \text{Re}/\beta^2$, and $\text{Rm}^* \equiv \text{Rm}/\beta^2$, in terms of which we carry out the following WKB analysis. It is easy to check that β disappears in the polynomial Eq. (4) after substituting these rescaled parameters (denoted with asterisks) in its coefficients.

Figure 1(a) shows the growth rate, $\text{Re}(\gamma)$, as a function of the rescaled axial wave number, as determined from a numerical solution of Eq. (4) at finite but very small $\text{Pm} = 10^{-6}$, together with solution (5) in the inductionless limit, for fixed Ha^* and Re^*. For the Rossby number, we take the values lower, $\text{Ro} = 1.5, 2$, and higher, $\text{Ro} = 6$, than Ro_{ULL}. Two distinct instability regimes are clearly seen in this figure. Type 2 Super-HMRI is concentrated at small k_z^* and exists at finite Pm both for $\text{Ro} < \text{Ro}_{ULL}$ and $\text{Ro} > \text{Ro}_{ULL}$; i.e., it is insensitive to the upper Liu limit, but disappears for $\text{Pm} \to 0$ at fixed Hartmann and Reynolds numbers. By contrast, type 1 Super-HMRI, concentrated at larger k_z^*, exists only for $\text{Ro} > \text{Ro}_{ULL}$, and approaches the inductionless solution as $\text{Pm} \to 0$. This latter branch is basically an extension of the more familiar HMRI operating at negative shear, which in the inductionless limit also satisfies Eq. (5), but at $\text{Ro} < \text{Ro}_{LLL}$, where $\text{Ro}_{LLL} = 2(1 - \sqrt{2}) \approx -0.83$ is the lower Liu limit [19,24,27].

At large $\text{Pm} \gg 1$, type 1 Super-HMRI disappears and there remains only type 2 Super-HMRI, as shown in Fig. 2(a). The corresponding dispersion curves as a function of axial wave number have a
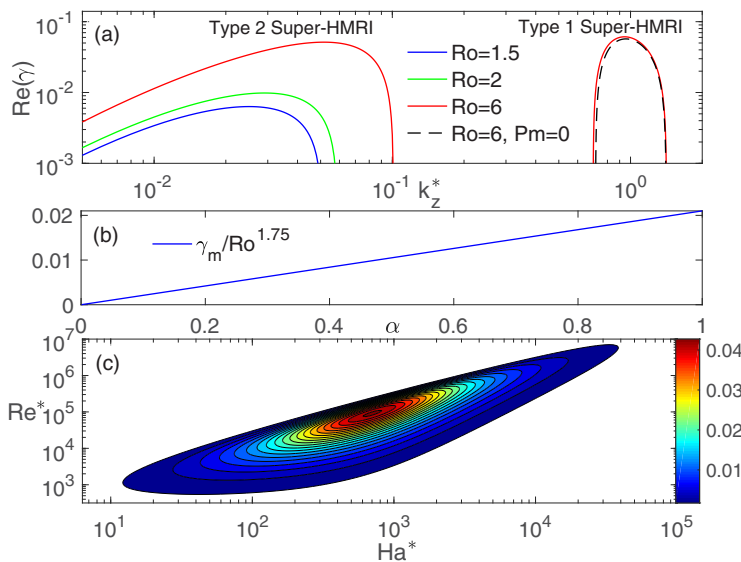
FIG. 1. Panel (a) shows the growth rate $\text{Re}(\gamma)$ vs k_z^* at fixed $\text{Ha}^* = 90$, $\text{Re}^* = 8 \times 10^3$, $\alpha = 0.71$ (i.e., $k_r^* = k_z^*$), and $\text{Pm} = 10^{-6}$ for different $\text{Ro} = 1.5$ (blue), 2 (green), 6 (red). Type 2 Super-HMRI branch exists at smaller k_z^* and finite Pm, for all three Ro values. By contrast, type 1 Super-HMRI branch at larger k_z^* appears only for $\text{Ro} = 6 > \text{Ro}_{ULL}$, but persists also in the inductionless limit [Eq. (5), dashed black line]. For the same Pm, panel (b) shows the growth rate of type 2 Super-HMRI, maximized over a set of the parameters (k_z^*, Ha^*, Re^*) and normalized by $\text{Ro}^{1.75}$, vs α, while panel (c) shows the growth rate, maximized over k_z^* and α, as a function of Ha^* and Re^* at $\text{Ro} = 1.5$ and the same $\text{Pm} = 10^{-6}$.

shape similar to those at small Pm in Fig. 1(a), but now the instability occurs at order of magnitude larger k_z^* and several orders of magnitude smaller Ha^* and Re^* at the same values of Ro adopted in these figures.

Thus, type 2 Super-HMRI represents a dissipation-induced instability mode at positive shear, which appears to require the presence of *both* finite viscosity and resistivity. As we will see below, though, it does not operate in the immediate vicinity of $\text{Pm} = 1$; that is, it is double-diffusive in nature, operating for both small and large Pm, but not for $\text{Pm} = O(1)$. Just as all previous MRI variants, this one also derives energy solely from the shear, since the imposed magnetic field is current-free, thereby eliminating current-driven instabilities, such as the Tayler instability. Energy is drawn from the background flow $r\Omega(r)$ to the growing perturbations due to the coupling between meridional circulation and azimuthal field perturbations brought about by the imposed azimuthal field, a mechanism also underlying HMRI at negative shear [6,29].

Our main goal is to describe the properties of this type 2 Super-HMRI. Type 1 Super-HMRI, existing only for $\text{Ro} > \text{Ro}_{ULL}$ and persisting even in the inductionless limit $\text{Pm} \to 0$ [19,23,24,28], is also interesting in its own right but will not be considered here further.

Like normal HMRI at negative shear, type 2 Super-HMRI is an overstability; that is, its growth rate comes with an associated nonzero imaginary part, $\omega = \text{Im}(\gamma)$, which is the frequency of temporal oscillations of the solution at a given coordinate and, together with axial wave number, defines its propagation speed. Figure 3 shows these frequencies as a function of k_z^*, corresponding to the growth rates plotted in Figs. 1(a) and 2(a). They monotonically increase with k_z^* by absolute value, but are positive at small Pm and negative at large Pm, implying opposite propagation directions of the wave patterns at these magnetic Prandtl numbers. Also, ω remains smaller than the frequency of inertial oscillations, $\omega_{io} = 2\alpha(1 + \text{Ro})^{1/2}$, and tends to the latter only at small Pm as the solution changes from type 2 to type 1 Super-HMRI with increasing k_z^* and does not change
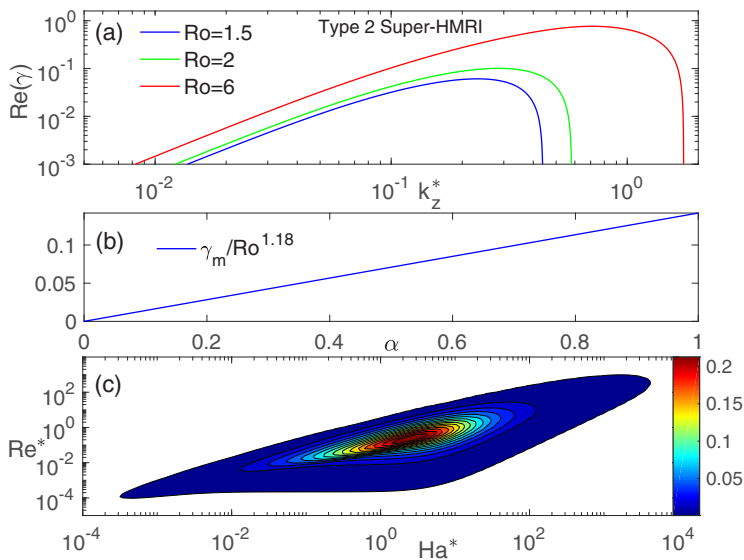
FIG. 2. Same as in Fig. 1, but at $Ha^* = 5$, $Re^* = 0.1$, $\alpha = 0.71$ in panel (a) and $Pm = 100$ in all panels. Type 2 Super-HMRI branch exists at higher k_z^* than those at small Pm, while type 1 Super-HMRI branch is absent. In panel (b), the maximum growth rate now exhibits the scaling with Rossby number, $Ro^{1.18}$, different from that at small Pm. In panel (c), the maximum growth occurs now at orders of magnitude smaller Ha_m^* and Re_m^* than those at small Pm in Fig. 1(c) at the same $Ro = 1.5$.

afterward. This reflects the fact that type 1 Super-HMRI represents weakly destabilized inertial oscillations, like the normal HMRI at negative shear [19].

To explore the behavior of type 2 Super-HMRI further, we first vary α as well as the rescaled Hartmann and Reynolds numbers. The growth rate, maximized over the last two numbers and k_z^*, increases linearly with α and scales as $\propto Ro^{1.75}$ at small $Pm = 10^{-6}$ [Fig. 1(b)] and as $\propto Ro^{1.18}$ at large $Pm = 100$ [Fig. 2(b)], while its dependence on Ha^* and Re^*, when maximized over k_z^* and α, is shown in Fig. 1(c) at $Pm = 10^{-6}$ and in Fig. 2(c) at $Pm = 100$ with $Ro = 1.5 < Ro_{ULL}$ (when type 1 Super-HMRI is absent) in both cases. The most unstable region is quite localized, with the growth rate decreasing for both small and large Ha^* and Re^*, implying that this instability relies on finite viscosity and resistivity; i.e., it is indeed of double-diffusive type. The overall shape of the unstable area in (Ha^*, Re^*) plane does not change qualitatively at other Pm and Ro; the unstable region always remains localized and shifts to larger Ha^* and Re^* with decreasing Pm. In particular, the maximum growth rate, γ_m, occurs for $(Ha_m^*, Re_m^*) \approx (700, 9 \times 10^4)$ when Pm is small [Fig. 1(c)], but for orders of magnitude smaller $(Ha_m^*, Re_m^*) = (2.54, 0.23)$ when Pm is large [Fig. 2(c)]. The actual values of the characteristic vertical wave number, Hartmann and Reynolds numbers for type 2 Super-HMRI at different β are obtained by simply multiplying the values of rescaled quantities k_z^*, Ha^*, Re^* given in Figs. 1 and 2 (as well as those in Fig. 4 of the following analysis) by β or β^2, respectively. For example, the largest growth rate at $Pm = 10^{-6}$ actually occurs at $(Ha_m, Re_m) = \beta(Ha_m^*, Re_m^* \beta) \approx \beta(700, 9 \times 10^4 \beta)$. These latter values can, in turn, be compared with the global stability analysis presented below as well as with magnetic Taylor-Couette (TC) flow experiments.

We next consider variation with Pm at fixed $Ro = 1.5 < Ro_{ULL}$, so that type 1 Super-HMRI is excluded. Figure 4 shows the growth rate γ_m, maximized over a set of parameters (α, k_z^*, Ha^*, Re^*) as well as the associated Ha_m^* and Re_m^*, at which this maximum growth is achieved, as a function of Pm. It is seen that for $Pm \lesssim 10^{-2}$, the growth rate is practically constant, $\gamma_m = 0.043$, while Ha_m^* and Re_m^* increase with decreasing Pm as the power laws $Ha_m^* \propto Pm^{-1/2}$ and $Re_m^* \propto Pm^{-1}$. So, in
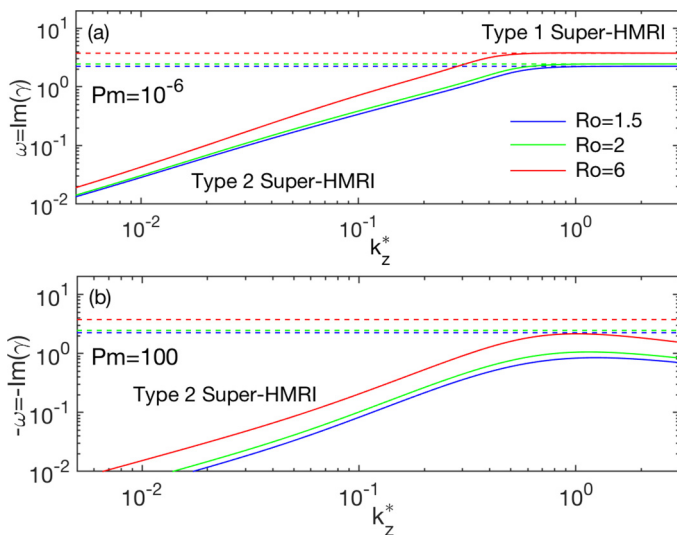
FIG. 3. Imaginary part of the eigenvalues, that is, frequency $\omega = \text{Im}(\gamma)$, at small $\text{Pm} = 10^{-6}$ (a) and large $\text{Pm} = 100$ (b) corresponding, respectively, to the growth rates shown in Figs. 1(a) and 2(a) at the same $\text{Ro} = 1.5$ (blue), $\text{Ro} = 2$ (green), $\text{Ro} = 6$ (red), and $\alpha = 0.71$. Dashed lines correspond to the frequency of inertial oscillations, $\omega_{io} = 2\alpha(1 + \text{Ro})^{1/2}$, for these parameters. Note that at small Pm the frequencies are positive, while at large Pm they are negative [$-\text{Im}(\omega)$ is plotted in panel (b)], implying opposite propagation directions of the wave patterns at these magnetic Prandtl numbers.

this small-Pm regime, type 2 Super-HMRI is more appropriately described in terms of Lundquist and magnetic Reynolds numbers, since these are $S_m^* = \text{Ha}_m^* \text{Pm}^{1/2} = 0.7$, $\text{Rm}_m^* = \text{Re}_m^* \text{Pm} = 0.091$, and thus independent of Pm. These scalings with S and Rm, being independent of Pm at $\text{Pm} \to 0$,

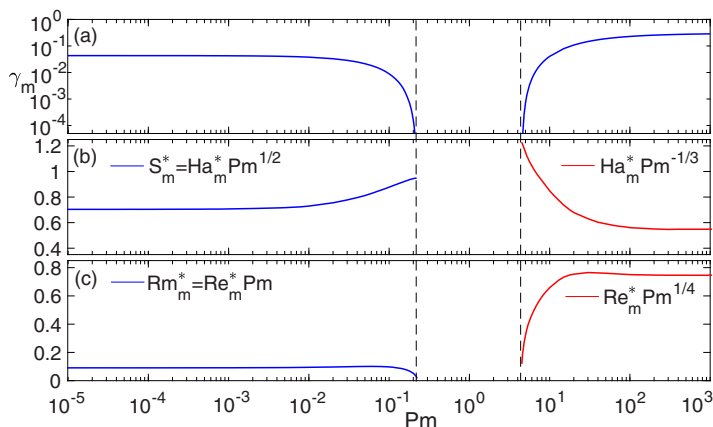FIG. 4. Panel (a) shows the growth rate, γ_m, of type 2 Super-HMRI, optimized over a set of parameters $(\alpha, k_z^*, \text{Ha}^*, \text{Re}^*)$ and represented as a function of Pm, at fixed $\text{Ro} = 1.5$. Panels (b) and (c) show the corresponding Ha_m^* and Re_m^*, respectively. For both $\text{Pm} \ll 1$ and $\text{Pm} \gg 1$, γ_m tends to constant values. The rescaled Hartmann and Reynolds numbers vary as $\text{Ha}_m^* \propto \text{Pm}^{-1/2}$ and $\text{Re}_m^* \propto \text{Pm}^{-1}$ for $\text{Pm} \ll 1$, and as $\text{Ha}_m^* \propto \text{Pm}^{1/3}$ and $\text{Re}_m^* \propto \text{Pm}^{-1/4}$ for $\text{Pm} \gg 1$. Panels (b) and (c) are compensated by these factors to more clearly highlight these scalings. The dashed lines are at $\text{Pm}_{c1} = 0.223$ and $\text{Pm}_{c2} = 4.46$, marking the $\text{Pm} = O(1)$ region where no instability exists.
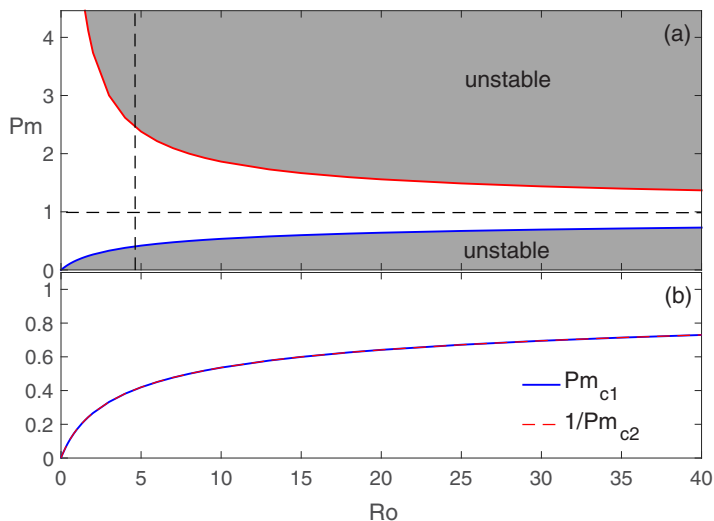
FIG. 5. Panel (a) shows the lower (Pm_{c1}, blue) and upper (Pm_{c2}, red) stability boundaries of type 2 Super-HMRI vs Ro. The vertical dashed line denotes the Liu limit $Ro_{ULL} = 4.83$. Panel (b) illustrates that these boundaries are in fact related by $Pm_{c1} = 1/Pm_{c2}$. Note that this instability exists for both smaller and larger Ro and in fact is insensitive to the upper Liu limit.

are similar to those of SMRI, and imply that this instability also does not exist in the inductionless limit, which would require S^*, $Rm^* \rightarrow 0$, and hence S, $Rm \rightarrow 0$, if Ha^* and Re^* are to remain finite.

With increasing Pm, beyond $Pm \sim 0.01$, γ_m rapidly decreases, and eventually the instability disappears at the first critical value $Pm_{c1} = 0.223$, with corresponding $(Ha_m^*, Re_m^*) = (2.018, 0.071)$ and the rescaled wave number $k_{zm}^* = 2.4 \times 10^{-3}$. It reappears again for larger $Pm > 1$ at the second critical value $Pm_{c2} = 4.46$, with $(Ha_m^*, Re_m^*) = (2, 0.046)$ and $k_{zm}^* = 5 \times 10^{-3}$, comparable to those at Pm_{c1}. Further increasing Pm, for $Pm \gtrsim 10$, γ_m eventually approaches a constant value 0.29. The corresponding rescaled Hartmann and Reynolds numbers again follow the power-law scalings, now $Ha_m^* \propto Pm^{1/3}$ and $Re_m^* \propto Pm^{-1/4}$.

Note that while we have only presented the $Ro = 1.5$ case in order to demonstrate the behavior of the instability with Pm, other values of Rossby number yield qualitatively similar behavior and scalings of γ_m, Ha_m^*, Re_m^*. Thus, the type 2 Super-HMRI exists over a broad range of magnetic Prandtl numbers, provided that viscosity ν and resistivity η are such that the immediate neighborhood of $Pm = 1$ is avoided, and $Pm < Pm_{c1} < 1$ or $Pm > Pm_{c2} > 1$.

Figure 5(a) shows the unstable regions of type 2 Super-HMRI in (Ro, Pm) plane. For all Ro, the two bounding curves of marginal stability where $\gamma_m = 0$ satisfy $Pm_{c1} < 1$ and $Pm_{c2} > 1$, and are related via $Pm_{c1}Pm_{c2} = 1$, as seen in Fig. 5(b). For high shear (Ro $\rightarrow \infty$), the stability strip around $Pm = 1$ increasingly narrows, so that most Pm values are unstable, whereas for Ro $\rightarrow 0$, the stable strip widens to include all Pm. This is readily understood, because shear is the only energy source (just as it is for SMRI, AMRI, and HMRI), and clearly there can be no instability at all for $Ro = 0$, which corresponds to solid-body rotation. Note finally how Pm_{c1} and Pm_{c2} stability curves are completely unaffected by the Liu limit at $Ro_{ULL} = 4.83$, which is only relevant to type 1 Super-HMRI. Hence, type 2 Super-HMRI continues to exist even for $Ro < Ro_{ULL}$.

Having described the properties of type 2 Super-HMRI using the WKB analysis, we should now address the question of validity of this approach. A basic condition for the local WKB approximation to hold is that the radial wavelength, λ_r, of the perturbations must be much smaller than the characteristic radial size, r_o, of the system over which the equilibrium quantities vary, i.e., $\lambda_r \ll r_o$. In terms of the radial wave number $k_r = 2\pi/\lambda_r$, this condition becomes $r_o k_r \gg 1$,

or in nondimensional units used here $k_r \gg 1$. From the above analysis [see Figs. 1(a) and 2(a)], it appears that the rescaled wave numbers typical of this instability are relatively small, $k_r^* \sim k_z^* \lesssim 0.1 - 1$. Recalling that $k_r = \beta k_r^*$, it follows that WKB approach is strictly applicable only at large $\beta \gg 1/k_r^* \gtrsim 10$, i.e., at dominant background azimuthal magnetic field. However, we will see in the global linear analysis below that this mode of instability is in fact not restricted only to large β and can even exist at smaller $\beta \sim 1$, but in this case the WKB approach is questionable and should be applied with caution.

IV. GLOBAL ANALYSIS

After the radially local WKB analysis, we now investigate type 2 Super-HMRI in the global case. The problem reduces to a 1D (along radius) linear eigenvalue problem in a viscous and resistive rotational flow between two coaxial cylinders threaded by helical magnetic field, as outlined in Ref. [6]. Hence, the main equations are the same as those in that paper and are obtained by linearizing Eqs. (1)–(3) about the above equilibrium, with the only difference being that now the imposed rotation profile $\Omega(r)$ increases with radius corresponding to outer cylinder rotating faster than the inner one (super-rotation). The boundary conditions are no slip for the velocity and either perfectly conducting or insulating for the magnetic field. As in Ref. [6] (see also Refs. [27,29]), the radial structure of the quantities are expanded in Chebyshev polynomials, typically up to $N = 30$–40. The governing equations and boundary conditions then reduce to a large ($4N \times 4N$) matrix eigenvalue problem, with the real parts of eigenvalues being growth rates of the eigenmodes and imaginary parts their frequencies (see also Ref. [30] for the details of the numerical scheme). In this paper, the global 1D analysis serves two main purposes: first, to compare with the results of the above WKB analysis in the regime where the latter holds, i.e., at high $\beta \gg 10$ and a small gap width between the cylinders, $\delta \equiv r_o - r_i \ll r_o$, when the equilibrium quantities do not change much with radius across the gap. Such an analysis will allow us to ascertain the existence of type 2 Super-HMRI also in the global setup and to characterize influence of the boundary conditions (conducting, insulating) for the magnetic field imposed on the cylinders. Second, with a view to detecting this instability in the upcoming liquid sodium TC experiments at the DRESDYN facility [31], we look for it at a larger gap width and smaller $\beta \sim 1$, a regime where WKB approximation becomes questionable, but, on the other hand, which is more relevant to experimental conditions. We start our global linear stability analysis with the first case.

A. Narrow-gap case

One of the main difficulties when comparing local and global analysis of HMRI and AMRI in a magnetic TC flow is that the local Rossby number, which defines these instabilities and to which they are therefore sensitive [19,23,24], varies with radius, even in the narrow gap case. On the other hand, it is assumed to be radially constant in the WKB treatment, as other equilibrium variables are. So, there is some uncertainty in matching Rossby numbers in the local and global analysis [14]. To circumvent this problem and facilitate comparison with the WKB analysis, following Ref. [32], we impose a power-law radial profile of angular velocity with a constant positive Rossby number,

$$\Omega(r) = \Omega_o \left(\frac{r}{r_o} \right)^{2\mathrm{Ro}} \tag{6}$$

(outer cylinder's $\Omega_o = 1$ in our units) as a background flow between the cylinders instead of the usual TC flow profile. The gap is assumed to be narrow with the ratio of inner to outer cylinders' radii $\hat{\eta} = r_i/r_o = 0.85$. The Rossby number is chosen smaller than the upper Liu limit, $\mathrm{Ro} = 3.5 < \mathrm{Ro}_{ULL}$, thereby excluding type 1 Super-HMRI in the global case too and allowing us to focus only on the type 2 Super-HMRI branch (the results are similar also at smaller Ro).

From the WKB analysis above, we have seen that for a given value of the growth rate, the associated wave numbers are proportional to the helicity parameter β. As a result, in order to confine

type 2 Super-HMRI within the gap extent in the global case and at the same time remain in the domain of validity of the WKB approximation, its radial wavelength should be at least comparable to or smaller than the gap width and, consequently, much smaller than the outer cylinder radius r_o. In terms of the radial wave number, this condition becomes $k_r \gtrsim \delta^{-1}$, which in our nondimensional units turns out to be large $k_r \gtrsim r_o \delta^{-1} = (1 - \hat{\eta})^{-1} \gg 1$, because the gap is narrow $\hat{\eta} \approx 1$ (similarly increases with β also the vertical wave number k_z). In terms of the rescaled wave numbers used in the WKB analysis, we get $\beta k_r^* \gtrsim (1 - \hat{\eta})^{-1} = 6.67$, with which we can estimate from Figs. 1(a) and 2(a) that in order to get such high wave numbers we arrive on the same constraint that β should be large, $\beta \gtrsim 100$ (for the adopted values of Ro and Pm). It also follows from Figs. 1(c) and 2(c) that due to the above scaling with β, the Hartmann and Reynolds numbers, for which the instability grows most, are accordingly also fairly high: Ha $\sim 10^4$, Re $\sim 10^9$ for small Pm $= 10^{-6}$ and Ha $\sim$ 100, Re $\sim 10^3$ for large Pm $= 100$. In order to avoid the numerical difficulties in our 1D eigenvalue code when both axial wave number and Reynolds number are such high ($k_z \gtrsim 10$ and Re $\sim 10^9$), we take higher Pm $= 10^{-3}$ in these global calculations at the narrow gap instead of Pm $= 10^{-6}$ used in Fig. 1. This, however, does not change the regime of the instability, because according to Fig. 4, we are still in the same asymptotic regime of low Pm $\ll 1$, where the growth rate is determined by S and Rm. As a result, the adopted Pm $= 10^{-3}$ yields lower values of Ha $\sim 10^3$ and Re $\sim 10^6$ for the same growth rate, which is computationally not as challenging. Such numerical problems do not arise for Pm $= 100$, where Re is three orders of magnitude lower, so we keep this value of the magnetic Prandtl number in the global analysis for the case when it is high and the gap is narrow.

Figures 6 and 7 present the results of the global calculations in the narrow gap case. Plotted here is the growth rate and frequency of type 2 Super-HMRI as a function of k_z at conducting and insulating boundary conditions for, respectively, small Pm $= 10^{-3}$ and large Pm $= 100$ and various pairs of (Ha, Re). For comparison, we also show the solutions of the WKB dispersion relation [Eq. (4)] at a fixed radial wave number $k_{r0} = \pi (1 - \hat{\eta})^{-1}$ in these figures. This choice of the radial wave number when comparing local results with 1D global ones is dictated by the fact that global eigenfunctions (see below) usually extend almost over the whole domain between the cylinders and do not change sign in the radial direction within this domain (see also Refs. [14,25]) [33]. It is seen that in all these cases both the frequency and growth rate of the instability exhibit generally a qualitatively similar dependence on the axial wave number as in the local analysis, with comparable maximum growth rates and corresponding k_{zm}; however, there is a noticeable quantitative difference between the small- and high-Pm regimes—the influence of the boundary conditions on the frequency and growth rate and hence deviations from the WKB results are larger at small Pm. The boundary conditions cause the dispersion curves for the growth rate to somewhat shift toward lower k_z, while those for the frequencies shift toward larger k_z relative to those in the local case. Besides, depending on Ha and Re, conducting boundaries can lead either to increase or decrease of the growth rate compared to its WKB value, whereas insulating boundaries always reduce the growth rate about three times compared to those for the conducting ones for fixed Hartmann and Reynolds numbers. As for the frequencies, they are quite close to each other for both boundary conditions and, at a given k_z, smaller than those in the local case. By contrast, for large Pm, the growth rate and frequency are essentially the same (dispersion curves are indistinguishable) for conducting and insulating boundaries (for this reason, Fig. 7 shows only the blue curves that represent both the boundary conditions) and quite close to their respective values from the WKB analysis, although with increasing Ha and Re the deviation from the local analysis becomes more noticeable, especially for the growth rate at smaller k_z [Fig. 7(c)]. This behavior with Pm is also consistent with previous studies on Super-AMRI at positive shear, indicating generally higher critical onset values of Hartmann and Reynolds numbers and, for given values of these numbers, smaller growth rates for insulating boundaries than those for conducting ones at smaller Pm, but almost identical critical values of Ha and Re and growth rates for both these boundary conditions at large Pm [16,34].

To better understand and interpret this behavior of type 2 Super-HMRI in the global case, we computed the associated spatial eigenfunctions. The structure of these eigenfunctions for the radial
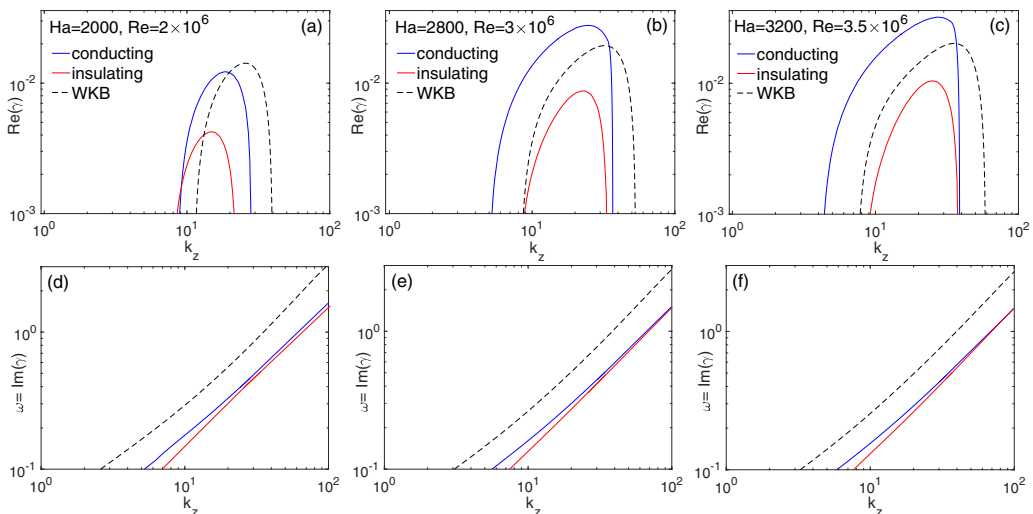
FIG. 6. Growth rate, $\mathrm{Re}(\gamma)$ [panels (a), (b), (c)], and frequency, $\omega = \mathrm{Im}(\gamma)$ [panels (d), (e), (f)], vs k_z in the global case with the narrow gap $\hat{\eta} = 0.85$ and power-law angular velocity profile with constant $\mathrm{Ro} = 3.5 < \mathrm{Ro}_{ULL}$ in the presence of conducting (blue) and insulating (red) boundary conditions imposed on the cylinders. In all panels, $\beta = 100$, $\mathrm{Pm} = 10^{-3}$, while $(\mathrm{Ha}, \mathrm{Re}) = (2000, 2 \times 10^6)$ in panels (a) and (d), $(\mathrm{Ha}, \mathrm{Re}) = (2800, 3 \times 10^6)$ in panels (b) and (e), and $(\mathrm{Ha}, \mathrm{Re}) = (3200, 3.5 \times 10^6)$ in panels (c) and (f). Black dashed curve in each panel is accordingly the growth rate or frequency resulting from the local WKB dispersion relation [Eq. (4)] for the same values of the parameters corresponding to that panel and a fixed $k_{r0} = \pi/\delta$, where $\delta = 1 - \hat{\eta}$ is the gap width in units of r_o. It is seen that in the local and global cases, the shape of the dispersion curves is qualitatively the same, with comparable growth rates, frequencies, and corresponding wave numbers; however, the boundary conditions tend to shift the growth rates toward lower axial wave numbers, while the frequencies toward larger wave numbers relative to those in the local case. Also, insulating boundaries lower the growth rate about three times. As for the frequencies, they are close to each other for both these boundaries and smaller than those in the local case at a given k_z.

and azimuthal components of the velocity and magnetic field in the (r, z) plane at small and large Pm, both for the conducting and insulating boundary conditions, are shown in Figs. 8–10. The values of axial wave numbers in each figure are chosen such that to get the largest growth rate for given values of the remaining parameters in Figs. 6(b) and 7(b), i.e., $k_{zm} = 24$ for conducting and $k_{zm} = 23$ for insulating boundaries at small $\mathrm{Pm} = 10^{-3}$, while at large $\mathrm{Pm} = 100$, we take $k_{zm} = 141$, which is the same for both the boundary conditions. First of all, we note that despite differences in structure, these eigenfunctions appear quite similar to those of the more familiar HMRI and AMRI in a TC setup with negative shear (e.g., Refs. [5–7,35,36]), extending over most part of the radial extent of the flow. They do not display any strong concentration in the vicinity of only the inner or outer radial boundaries, which would otherwise mean that the instability mode is induced due to those boundaries. Thus, although the radial boundaries, either insulating or conducting, affect the growth rate, especially at small Pm (Fig. 6), they are not the main cause or driver of type 2 Super-HMRI. It is the combination of shear, helical magnetic field and dissipation that gives rise to this instability. In this regard, it is already known that the type of radial boundary conditions for the magnetic field also plays an important role in the dynamics of more extensively studied "relatives"—axisymmetric and nonaxisymmetric AMRI at negative shear [29,32,34], whose basic physics can be understood also within the local WKB analysis [19,22–24,27].

It is seen in these figures that the eigenfunctions markedly differ in structure depending on the magnetic Prandtl number and boundary conditions. At $\mathrm{Pm} = 10^{-3}$, they appear to have comparable axial and radial length scales, which are of the same order as the radial size of the gap, with the radial
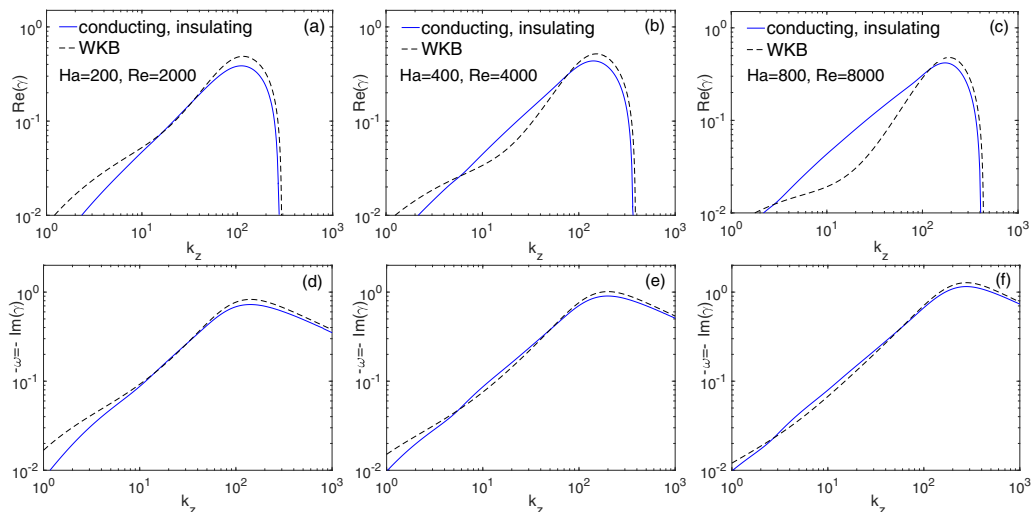
FIG. 7. Same as in Fig. 6, but at large Pm = 100 with (Ha, Re) = (200, 2000) in panels (a) and (d), (Ha, Re) = (400, 4000) in panels (b) and (e), and (Ha, Re) = (800, 8000) in panels (c) and (f). Note that in this case the growth rates and frequencies [plotted is $-\omega = -\text{Im}(\gamma)$] are nearly indistinguishable for conducting and insulating boundary conditions, in contrast to the small-Pm regime depicted in Fig. 6. Black dashed curve in each panel is again the growth rate or frequency resulting from the WKB dispersion relation [Eq. (4)] with $k_{r0} = \pi/\delta$ and the same values of the parameters corresponding to that panel. For the growth rate, the difference between the local and global dispersion curves increases with increasing Hartmann and Reynolds numbers mainly at smaller $k_z \lesssim 10$ [panel (c)], whereas for the frequencies these curves are quite close to each other. Overall, the agreement between the WKB and 1D analysis at large Pm = 100 is much better than that at small Pm = 10^{-3} in Fig. 6.

scale of the velocities being somewhat smaller than that of the magnetic field (Figs. 8 and 9). This implies that (i) the effective radial wave numbers for these components are slightly different, which can explain the deviation from the WKB result seen in Fig. 6, as the velocity and magnetic field perturbations should have a common radial wave number in the local case (although formally the condition for the WKB approximation—r_o is larger than the radial length scale of the perturbation—is satisfied) and (ii) the boundary conditions on the cylinders do play a role in determining the structure of the eigenfunctions and therefore can modify the growth rate of the instability. Indeed, it is seen in Figs. 8 and 9 that the insulating boundaries introduce more smaller scale features in the eigenfunctions, especially in the velocity ones, compared to those in the presence of the conducting boundaries, which apparently leads to the difference in the corresponding growth rates in Fig. 6.

The situation is different in the case of large Pm = 100 shown in Fig. 10 in that the axial length scale of the eigenfunctions is much smaller than the radial one, which is again comparable to the gap width, i.e., $k_{zm} \gg \lambda_r^{-1} \sim \delta^{-1}$ (for the ease of comparison, the same range in z is used in all panels in Figs. 8–10). It is seen from this figure that unlike the case of small Pm, now the structure of the velocity and magnetic field eigenfunctions and hence their effective radial wave numbers are very similar. Since this effective radial wave number turns out to be much smaller than k_{zm}, to a zeroth-order approximation the eigenfunctions can be assumed to be radially independent and vary only along z. In this case, however, calculating the growth rate, one arrives at the same WKB dispersion relation [Eq. (4)] (when $k_r \ll k_z$, $\alpha \approx 1$). This implies that actually the WKB regime is better fulfilled at large Pm and those higher k_z, at which the instability reaches a maximum growth, and hence specific boundary conditions do not affect its growth and frequency. This can also explain the better agreement between the dispersion curves from the WKB and global analyses in Fig. 7 than that in Fig. 6. As a result, the structures of the eigenfunctions are also similar for both conducting
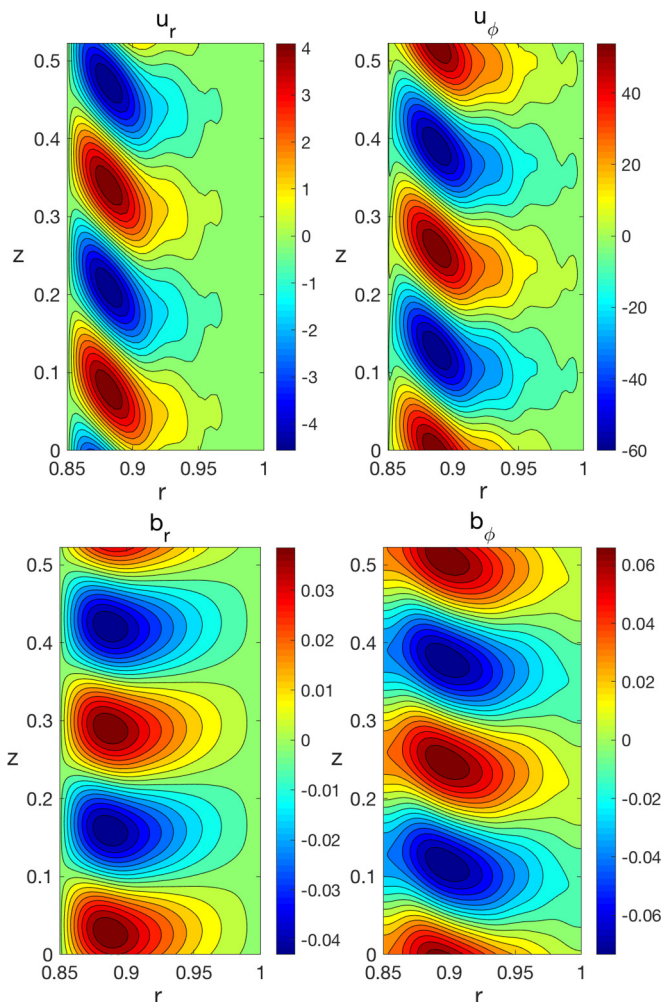
FIG. 8. Eigenfunctions of the radial and azimuthal velocity and magnetic field for type 2 Super-HMRI in the global case as a function of (r, z) at small Pm $= 10^{-3}$, the narrow gap $\hat{\eta} = 0.85$, and conducting boundary conditions on the cylinders. The parameters (β, Ro, Ha, Re) are the same as those in Fig. 6(b) and the axial wave number is chosen to be $k_{zm} = 24$, at which the growth rate for the given values of these parameters reaches a maximum (peak on the blue curve in that panel).

and insulating boundaries. For this reason, we show only the case with the conducting boundaries in Fig. 10, leading to nearly identical dispersion curves in Fig. 7.

This comparative local and 1D global analysis of type 2 Super-HMRI, for the conducting and insulating boundary conditions, in the narrow gap case, allowed us, first of all, to clearly demonstrate the existence of this double-diffusive instability also in the global setup of a differentially rotating dissipative flow with positive shear threaded by helical magnetic field. We have shown that the basic dependence of its growth rate and frequency on the flow parameters and axial wave number can still be understood and reproduced qualitatively within the local WKB approach. This indicates that type 2 Super-HMRI, like HMRI at negative shear, is a genuine instability intrinsic to the flow, tapping free energy of differential rotation (shear), and is *not* induced or driven by the radial boundaries on the confining rotating cylinders, although it can still be modified by these boundaries. We have seen above that the quantitative differences between the results of the WKB and global analyses
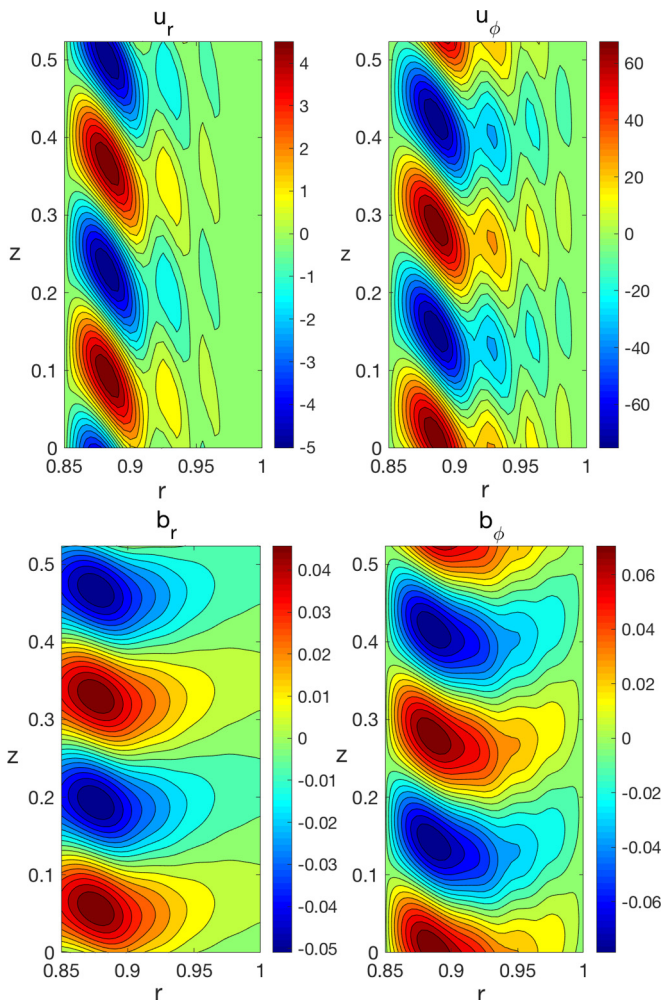
FIG. 9. Same as in Fig. 8, but for insulating boundary conditions on the cylinders. The main parameters are again the same as in Fig. 6(b), but now the axial wave number is chosen to be $k_{zm} = 23$, corresponding to the largest growth rate for the given values of these parameters (peak on the red curve in that panel) and the boundary conditions.

and some influence of specific radial boundary conditions on the growth rate and structure of the eigenfunctions are more noticeable at small magnetic Prandtl numbers but diminish at large Prandtl numbers, because when increasing this number the eigenfunctions tend to vary much more along the axial z direction than along the radial direction. Consequently, the WKB approximation holds much better in the latter case.

B. Wide-gap case

Having explored type 2 Super-HMRI in the local and narrow-gap global cases, we now look for it in the case of a wide gap. As noted above, in this subsection, the primary goal of these calculations is to identify this instability in a TC flow setup commonly employed in laboratory experiments, which in the present case has a radially increasing angular velocity (positive shear) profile. For this purpose, following Refs. [15,16,34], where the related Super-AMRI is studied in a TC flow at
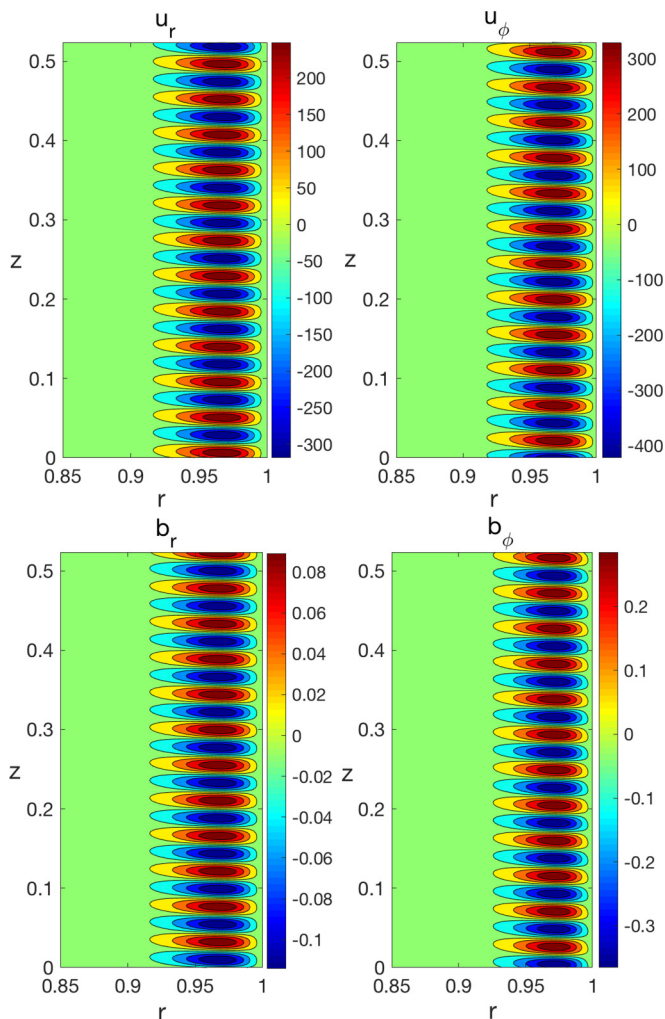
FIG. 10. Same as in Fig. 8, but for large Pm = 100 and conducting boundary conditions. The parameters $(\beta, \mathrm{Ro}, \mathrm{Ha}, \mathrm{Re})$ are the same as in Fig. 7(b) and the axial wave number is $k_{zm} = 141$, corresponding to the maximum growth rate (peak on the blue curve in that panel) for the given values of these parameters. For the sake of comparison of the eigenfunction structures and length scales with those at small Pm, the z axis has the same range as in Figs. 8 and 9. At large Pm, the eigenfunctions in the presence of insulating boundaries are in fact nearly identical to the ones for the conducting boundaries shown here at the same values of the main parameters and hence we do not plot those eigenfunctions.

positive shear, we adopt here one of the radial profiles for the angular velocity used in those papers, which is different from expression (6) at constant Ro. Specifically, the inner cylinder is assumed to be stationary, $\Omega_i = 0$, while the outer cylinder rotates at Ω_o, achieving a radially increasing angular velocity profile between the cylinders with the largest positive shear for a given rotation rate of the outer cylinder,

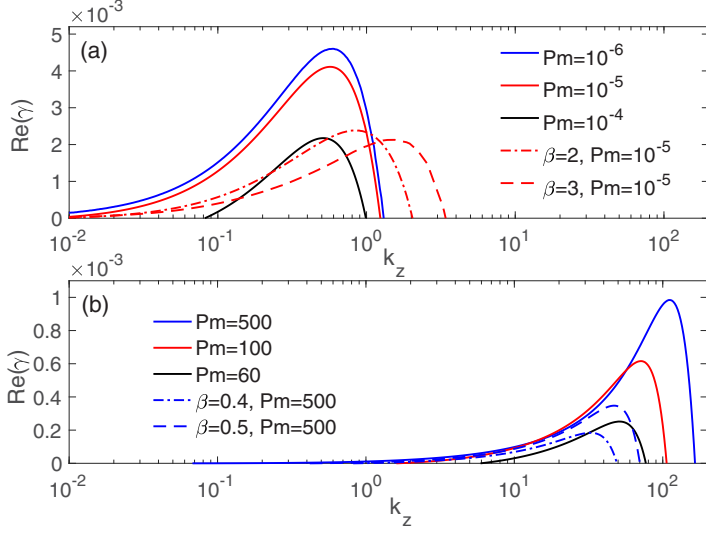$$\Omega(r) = \frac{\Omega_o}{1 - \hat{\eta}^2} \left(1 - \frac{r_i^2}{r^2} \right),$$

FIG. 11. Growth rate Re(γ) vs k_z for the TC flow with the wide gap, $\hat{\eta} = 0.5$, and the inner cylinder at rest. Panel (a) focuses on Pm $\ll 1$, with solid lines having fixed $\beta = 1$, $S = 4$, and Rm = 20 but different Pm, dot-dashed line $\beta = 2$, $S = 8$, Rm = 80, Pm = 10^{-5}, and dashed line $\beta = 3$, $S = 12$, Rm = 180, Pm = 10^{-5}. Panel (b) focuses on Pm $\gg 1$, with solid lines having fixed $\beta = 1$, Ha = 1600, and Re = 8×10^4 but different Pm, dot-dashed line $\beta = 0.4$, Ha = 640, Re = 1.28×10^4, Pm = 500, and dashed line $\beta = 0.5$, Ha = 800, Re = 2×10^4, Pm = 500.

where for the ratio of the inner to outer cylinders' radii we take the fixed value $\hat{\eta} = 0.5$ relevant to the TC devices in the PROMISE and DRESDYN experiments [9,31]. We take $\beta \sim 1$ in these calculations for the wide gap, since it is rather costly to achieve large β in experiments due to the very high axial currents required. In this wide-gap case, we impose conducting boundary conditions for the magnetic field on the cylinders. Note also that at $\beta = 1$ the rescaled parameters are equal to their actual counterparts: $k_z^* = k_z$, Ha* = Ha, Re* = Re, which is more convenient, and allows us to directly compare the results at wider gap with the local ones presented in Figs. 1 and 2.

Figure 11 shows the growth rate Re(γ) as a function of the wave number k_z for both small and large Pm, clearly demonstrating the presence of type 2 Super-HMRI also at a wide gap in the magnetic TC flow with radially increasing angular velocity. For $\beta = 1$, the instability is concentrated mainly at small $k_z \lesssim 1$ for Pm $\ll 1$ and shifts to larger $k_z \gtrsim 10$ for Pm $\gg 1$ as it does in the local analysis [Figs. 1(a) and 2(a)]. Note also that here the solutions explicitly depend on β, since the radial coordinate appears in the governing equations [6], unlike in the local analysis where β effectively scales out. However, as seen in Fig. 4, qualitatively the expected scalings with β are still followed, with Ha and Re (or S and Rm) as well as k_{zm} increasing with β.

Note also in Fig. 11(a) how three solid curves, corresponding to small Pm, converge as Pm decreases. This is consistent with the previous local analysis result that the relevant defining parameters in this case are Lundquist, S, and magnetic Reynolds, Rm, numbers, since they are kept fixed for these three curves. Figure 12 focuses further on this small magnetic Prandtl number case, as it is more relevant to TC experiments employing liquid metals (gallium, sodium) with Pm $\sim 10^{-6}$–10^{-5} [8–10], and shows how the growth rate, maximized over k_z, varies with S and Rm at fixed $\beta = 1$. Just as in Fig. 1(c) of the local analysis, the instability is again localized in the (S, Rm) plane, with the overall maximum growth rate, $\gamma_m = 4.8 \times 10^{-3}$, occurring at $S_m = 5.2$ and Rm$_m = 25$ (Ha$_m = 5.2 \times 10^3$ and Re$_m = 2.5 \times 10^7$). The minimum, or critical values for the instability to first emerge are $S_c \approx 0.3$ and Rm$_c \approx 0.9$. These values are well within the capabilities of the new TC device at HZDR [31], offering a realistic prospect for experimental realization and
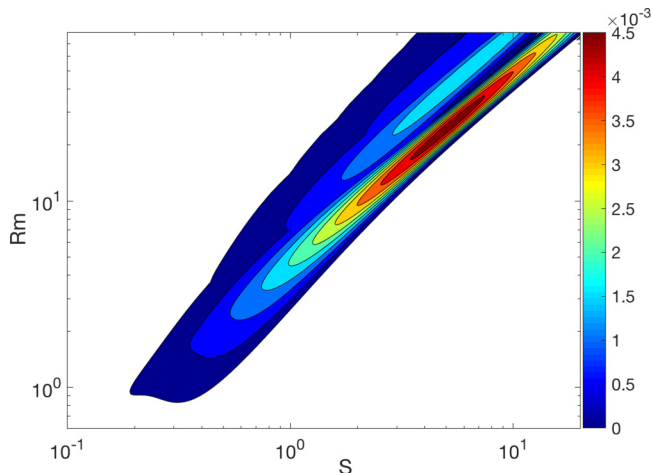
FIG. 12. Growth rate for the TC flow with the positive shear and wide gap, maximized over k_z and represented in the (S, Rm) plane, at fixed $\text{Pm} = 10^{-6}$ and $\beta = 1$. As in the local equivalent [Fig. 1(c)], the unstable region is localized in (S, Rm) plane, reaching a maximum at $S_m = 5.2$ and $\text{Rm}_m = 25$.

detection of type 2 Super-HMRI. However, since at $\beta \sim 1$ type 2 Super-HMRI occurs at smaller k_z [Figs. 11(a)], as far as the experimental detection is concerned, optimization with respect to β is required in order to ensure that the largest critical $k_{z,\max}$ of the instability, corresponding to the smallest wave number $\lambda_{z,\min} = 2\pi / k_{z,\max}$, still fits into the device, that is, $\lambda_{z,\min} \leqslant L_z$, where L_z is its vertical size. Such an optimization procedure and a more detailed analysis addressing the experimental manifestation of this instability will be presented elsewhere.

Although the results at wider gaps are qualitatively similar to those at local ones, there are noticeable quantitative differences in that the local analysis yields about an order of magnitude higher growth rate, but lower axial wave number and Hartmann number and about two orders of magnitude lower Reynolds number for the instability. This mismatch is expected, since in this case of $\beta \approx 1$, as mentioned above, the WKB approximation is inapplicable. The radial and axial length scales of the eigenfunctions are comparable to the gap width as well as to the radial size of the flow system, $\lambda_z \sim \lambda_r \sim \delta = r_i = 0.5 r_o$) and therefore the equilibrium appreciably varies over the whole radial extent of the mode. By contrast, the local WKB analysis better applies in the narrow-gap case, $\hat{\eta} \to 1$, because the eigenfunctions vary mostly only over the gap width (Figs. 8–10), which is much less than r_o and hence the radial variation of the equilibrium quantities are small across this distance. Another reason for the differences in the growth rates between the local and the global wide gap cases is that a finite distance between the cylinders also excludes (cuts off) very small radial wave numbers ($\alpha \to 1$), which correspond to larger growth rates at $\beta \sim 1$ in the WKB analysis [see Fig. 1(b)].

The primary purpose of these 1D global calculations for the narrow and wide gaps, supplementing the local analysis, has been to demonstrate the existence of this double-diffusive type 2 Super-HMRI at positive shear in the global setup too. A more comprehensive global linear analysis of this instability, exploring the dependence of its growth rate on the flow parameters $(\hat{\eta}, \beta, \text{Re}, \text{Ha}, \text{Pm})$, will be presented elsewhere. We also plan to explore the effects of boundary conditions, conducting versus insulating, in more detail at wide gap $\hat{\eta} = 0.5$, since, as we have seen in the narrow-gap case, they can lead to quite different onset criteria and growth rates of type 2 Super-HMRI, as it generally happens for MRI-type instabilities in TC flows (see, e.g., Refs. [7,34]). Such a study will be important for setting up a series of tailored TC experiments with radially increasing angular velocity at the DRESDYN facility, aiming at detecting type 2 Super-HMRI.

V. SUMMARY AND DISCUSSION

In this paper, we have uncovered and analyzed a type of double-diffusive axisymmetric HMRI, labeled type 2 Super-HMRI, which exists in rotational flows with radially increasing angular velocity, or positive shear of arbitrary steepness threaded by a helical magnetic field—a configuration where magnetorotational instabilities were previously unknown. The only prerequisites are that Pm $\neq$ 1 and the imposed magnetic field includes *both* axial and azimuthal components. First, we identified this instability using the radially local WKB analysis and subsequently ascertained its existence via 1D global linear stability analysis by solving a boundary value problem with conducting or insulating boundary conditions on the rotating cylindrical walls containing the flow. In the global setup, we separately considered the cases of narrow gap and large azimuthal field, in order to compare them with the results of the WKB analysis, and a wide gap and moderate azimuthal field, which is more relevant to experiments. The comparative analysis in the narrow-gap case indicates that although the global and local WKB results are qualitatively similar, there are quantitative differences in the growth rates and associated axial wave numbers mostly at small magnetic Prandtl numbers, since the radial and axial length scales of the modes are comparable to each other and to the gap width, and hence boundary conditions appear to modify the growth rate. By contrast, in the case of large Prandtl numbers, axial length scale of the mode is much smaller than the radial one (which is again comparable to the gap width) and consequently the influence of the boundaries is not important and the agreement with the WKB analysis is much better. In any case, the radial extent of the mode is always comparable to the gap width between the cylinders; i.e., it is concentrated within the bulk of the flow and not near either of the boundaries, indicating that type 2 Super-HMRI is in fact intrinsic to the flow system and is not induced due to specific boundary conditions. In this way, the global stability analysis also confirms that this instability is a real one and not just an artifact of the WKB approximation.

From an experimental perspective, in the wide-gap case, we have also demonstrated the presence of type 2 Super-HMRI in a magnetized viscous and resistive TC flow with positive shear, helical magnetic field, and such values of $\hat{\eta}$, β, Ha, Re, Pm, which can be well achieved in a liquid metal laboratory. This promising result of the global stability analysis can, in turn, be a basis for future efforts aiming at the detection of this instability and thereby providing an experimental evidence for its existence. This will also allow us to make comparison with theoretical results. Building on the findings of this study, future work will explore in greater detail the parameter space and the effect of boundary conditions on type 2 Super-HMRI, which are more relevant to those present in TC flow experiments.

Applicability to the solar tachocline

MRI has already been discussed in relation to the solar tachocline in several studies [17,37–40], showing that it can arise at middle and high latitudes, where the shear of the differential rotation is negative. The resulting small-scale MRI turbulence is thought to prevent coherent magnetic dynamo action in these regions of the tachocline, thus explaining the rare occurrence or absence of the sunspots at these latitudes.

The double-diffusive type 2 Super-HMRI, on the other hand, may arise and potentially have important implications for the dynamics and magnetic activity of the low-latitude, near-equatorial region of the solar tachocline, since necessary conditions for the development of this instability are realized there. Indeed, in this part of the tachocline, we have (i) the positive radial shear of differential rotation with Ro $\sim$ 0.1–1 [17,18], (ii) small magnetic Prandtl numbers Pm $\sim$ 0.01 [41–43], (iii) very high Reynolds numbers (inverse of often-used Ekman number), Re $\sim 10^{11}$–10^{14} [18,42,44], which are, of course, too challenging to use in theoretical and numerical studies, so lower values Re $\gtrsim 10^6$ are usually adopted instead (e.g., Refs. [43,45]), and (iv) helical magnetic field. Regarding the magnetic field, MHD models of the solar tachocline (e.g., Refs. [43,46,47] and references therein) also indicate that poloidal magnetic field in the tachocline should be relatively
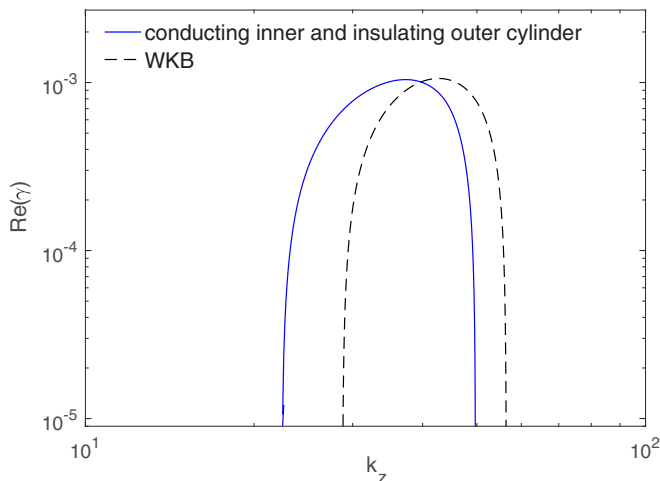
FIG. 13. Growth rate of type 2 Super-HMRI vs k_z for a power-law radial profile of the angular velocity with Ro = 0.7 and a very narrow gap $\hat{\eta} = 0.94$, which are close to those of the solar tachocline. The boundary conditions are conducting at the inner and insulating at the outer walls, as often used in solar tachocline studies. The other parameters are taken as follows (see text): $\beta = 500$, Pm = 0.01, Ha = 2500, and Re = 1.5×10^6. As in Fig. 6, black dashed line shows the WKB result for these parameters, but at much higher radial wave number $k_{r0} = \pi(1 - \hat{\eta})^{-1} \approx 52.4$, corresponding to a narrower gap.

large in order to produce a thin tachocline layer and therefore have large Hartmann numbers Ha $\sim 10^3$, while the toroidal magnetic field should be even stronger, several orders of magnitude higher than the poloidal one, resulting in very large β values. In practice, theoretical and numerical studies often use $\beta \sim 10^2$–10^3 (e.g., Refs. [48,49]), which in our case would ensure that the mode is confined within a fairly thin layer of the tachocline, which has a typical ratio of the inner to outer radii $\hat{\eta} \approx 0.9$–0.97 [50].

To demonstrate that the type 2 Super-HMRI can indeed arise in the tachocline-like configuration described above and thus to get a flavor of its amplification efficiency and characteristic wave number in this case, in Fig. 13 we show the growth rate as a function of k_z obtained from an analogous 1D global stability analysis as in the narrow-gap case of Sec. IV, assuming a power-law radial profile for the angular velocity [Eq. (6)] with smaller Ro = 0.7, narrower gap $\hat{\eta} = 0.94$, and the values of the remaining parameters also of the same order as those quoted above for the tachocline. As distinct from the above analysis, now we impose the boundary conditions often used in tachocline studies, namely conducting at the inner and insulating at the outer radius, mimicking, respectively, the conducting radiative interior and insulating convection zones in the Sun (e.g., Refs. [45,46,51]. It can be seen from this figure that the largest growth rate is $\approx 10^{-3}$, or in dimensional variables $\approx 10^{-3} \Omega_o$, and therefore the corresponding growth time is $\approx 10^3 \Omega_o^{-1}$. Taking into account that the Sun's angular velocity of rotation in the near-equatorial region of the tachocline is about $\Omega_o \approx 2\pi \times 445$ nHz = 88.2 yr^{-1} [52], for the characteristic growth time of this instability we get ≈ 11 yr, which is surprisingly close to the solar cycle period. This suggests that type 2 Super-HMRI can be quite relevant to the magnetic activity in the tachocline and generally in the Sun.

Although these calculations regarding the applications to the solar tachocline are simplistic, still remaining within the cylindrical rotational flow, they are nevertheless encouraging and motivate us to investigate in more detail the possible role of type 2 Super-HMRI in the dynamics, transport processes, and dynamo action in the tachocline using its more realistic model involving spherical (shell) geometry, radially and meridionally varying angular velocity (those parts where shear is positive, Ro > 0) and magnetic field distribution and boundary conditions. Such a comprehensive

study will allow us also to characterize in depth the potential implications of type 2 Super-HMRI in the dynamical processes in the tachocline. In particular, this instability could also resurrect the idea of a subcritical solar dynamo. Its axisymmetric ($m = 0$) nature can help to overcome the difficulties that have been identified [53] in getting the so-called Tayler-Spruit dynamo [54] to form a closed dynamo loop from the combination of the nonaxisymmetric ($m = 1$) Tayler instability and the $m = 0$ Ω-effect. Finding out whether this scenario is actually realized requires a further dedicated study using these more realistic tachocline models and is a subject of future work. In this connection, we would like to mention that an analogous mechanism for explaining solar magnetic cycles was put forward in Ref. [55], where the combined effect of differential rotation and axisymmetric current-driven instability can cause equatorward propagating reversals of the large-scale azimuthal field in the tachocline and convection zone, as is observed in the Sun, without relying on a classical α effect of mean-field dynamo theory.

[1] L. Rayleigh, On the dynamics of revolving fluids, Proc. R. Soc. London, Ser. A **93**, 148 (1917).

[2] E. Velikhov, Stability of an ideally conducting liquid flowing between rotating cylinders in a magnetic field, Sov. Phys. JETP **9**, 995 (1959).

[3] S. Chandrasekhar, The stability of non-dissipative Couette flow in hydromagnetics, Proc. Nat. Acad. Sci. USA **46**, 253 (1960).

[4] S. A. Balbus and J. F. Hawley, A powerful local shear instability in weakly magnetized disks. I. Linear analysis, Astrophys. J. **376**, 214 (1991).

[5] R. Hollerbach, V. Teeluck, and G. Rüdiger, Nonaxisymmetric Magnetorotational Instabilities in Cylindrical Taylor-Couette Flow, Phys. Rev. Lett. **104**, 044502 (2010).

[6] R. Hollerbach and G. Rüdiger, New Type of Magnetorotational Instability in Cylindrical Taylor-Couette Flow, Phys. Rev. Lett. **95**, 124501 (2005).

[7] G. Rüdiger, M. Gellert, R. Hollerbach, M. Schultz, and F. Stefani, Stability and instability of hydromagnetic Taylor-Couette flows, Phys. Rep. **741**, 1 (2018).

[8] M. Seilmayer, V. Galindo, G. Gerbeth, T. Gundrum, F. Stefani, M. Gellert, G. Rüdiger, M. Schultz, and R. Hollerbach, Experimental Evidence for Nonaxisymmetric Magnetorotational Instability in a Rotating Liquid Metal Exposed to an Azimuthal Magnetic Field, Phys. Rev. Lett. **113**, 024505 (2014).

[9] F. Stefani, T. Gundrum, G. Gerbeth, G. Rüdiger, M. Schultz, J. Szklarski, and R. Hollerbach, Experimental Evidence for Magnetorotational Instability in a Taylor-Couette Flow Under the Influence of a Helical Magnetic Field, Phys. Rev. Lett. **97**, 184502 (2006).

[10] F. Stefani, G. Gerbeth, T. Gundrum, R. Hollerbach, J. Priede, G. Rüdiger, and J. Szklarski, Helical magnetorotational instability in a Taylor-Couette flow with strongly reduced Ekman pumping, Phys. Rev. E **80**, 066303 (2009).

[11] D. R. Sisan, N. Mujica, W. A. Tillotson, Y.-M. Huang, W. Dorland, A. B. Hassam, T. M. Antonsen, and D. P. Lathrop, Experimental Observation and Characterization of the Magnetorotational Instability, Phys. Rev. Lett. **93**, 114502 (2004).

[12] M. D. Nornberg, H. Ji, E. Schartman, A. Roach, and J. Goodman, Observation of Magnetocoriolis Waves in a Liquid Metal Taylor-Couette Experiment, Phys. Rev. Lett. **104**, 074501 (2010).

[13] K. Deguchi, Linear instability in Rayleigh-stable Taylor-Couette flow, Phys. Rev. E **95**, 021102(R) (2017).

[14] F. Stefani and O. N. Kirillov, Destabilization of rotating flows with positive shear by azimuthal magnetic fields, Phys. Rev. E **92**, 051001(R) (2015).

[15] G. Rüdiger, M. Schultz, M. Gellert, and F. Stefani, Subcritical excitation of the current-driven Tayler instability by super-rotation, Phys. Fluids **28**, 014105 (2016).

[16] G. Rüdiger, M. Schultz, M. Gellert, and F. Stefani, Azimuthal magnetorotational instability with super-rotation, J. Plasma Phys. **84**, 735840101 (2018).

[17] K. P. Parfrey and K. Menou, The origin of solar activity in the tachocline, Astrophys. J. **667**, L207 (2007).

[18] S. M. Tobias, P. H. Diamond, and D. W. Hughes, β-plane magnetohydrodynamic turbulence in the solar tachocline, Astrophys. J. **667**, L113 (2007).

[19] W. Liu, J. Goodman, I. Herron, and H. Ji, Helical magnetorotational instability in magnetized Taylor-Couette flow, Phys. Rev. E **74**, 056302 (2006).

[20] M. A. Belyaev, R. R. Rafikov, and J. M. Stone, Angular momentum transport and variability in boundary layers of accretion disks driven by global acoustic modes, Astrophys. J. **760**, 22 (2012).

[21] M. E. Pessah and C.-K. Chan, On hydromagnetic stresses in accretion disk boundary layers, Astrophys. J. **751**, 48 (2012).

[22] O. N. Kirillov, F. Stefani, and Y. Fukumoto, A unifying picture of helical and azimuthal magnetorotational instability, and the universal significance of the Liu limit, Astrophys. J. **756**, 83 (2012).

[23] O. N. Kirillov, F. Stefani, and Y. Fukumoto, Local instabilities in magnetized rotational flows: a short-wavelength approach, J. Fluid Mech. **760**, 591 (2014).

[24] O. N. Kirillov and F. Stefani, On the relation of standard and helical magnetorotational instability, Astrophys. J. **712**, 52 (2010).

[25] H. Ji, J. Goodman, and A. Kageyama, Magnetorotational instability in a rotating liquid metal annulus, Mon. Notices Royal Astron. Soc. **325**, L1 (2001).

[26] J. Goodman and H. Ji, Magnetorotational instability of dissipative Couette flow, J. Fluid Mech. **462**, 365 (2002).

[27] J. Priede, Inviscid helical magnetorotational instability in cylindrical Taylor-Couette flow, Phys. Rev. E **84**, 066314 (2011).

[28] G. Mamatsashvili and F. Stefani, Linking dissipation-induced instabilities with nonmodal growth: The case of helical magnetorotational instability, Phys. Rev. E **94**, 051203(R) (2016).

[29] J. Priede, I. Grants, and G. Gerbeth, Inductionless magnetorotational instability in a Taylor-Couette flow with a helical magnetic field, Phys. Rev. E **75**, 047303 (2007).

[30] R. Hollerbach, Spectral solutions of the MHD equations in cylindrical geometry, Int. J. Pure Appl. Math. **42**, 575 (2008).

[31] F. Stefani, A. Gailitis, G. Gerbeth, A. Giesecke, T. Gundrum, G. Rüdiger, M. Seilmayer, and T. Vogt, The DRESDYN project: Liquid metal experiments on dynamo action and magnetorotational instability, Geophys. Astrophys. Fluid Dyn. **113**, 51 (2019).

[32] G. Rüdiger and R. Hollerbach, Comment on Helical magnetorotational instability in magnetized Taylor-Couette flow,, Phys. Rev. E **76**, 068301 (2007).

[33] Actually, the selected value of k_{r0} when comparing local WKB and global dispersion curves is still somewhat arbitrary, since it is not generally possible to get an exact matching between the characteristic radial length of the global eigenfunctions and radial wave number of WKB solutions and harmonics.

[34] G. Rüdiger, M. Schultz, F. Stefani, and R. Hollerbach, Magnetorotational instability in Taylor-Couette flows between cylinders with finite electrical conductivity, Geophys. Astrophys. Fluid Dyn. **112**, 301 (2018).

[35] A. Guseva, A. P. Willis, R. Hollerbach, and M. Avila, Transition to magnetorotational turbulence in Taylor-Couette flow with imposed azimuthal magnetic field, New J. Phys. **17**, 093018 (2015).

[36] G. Mamatsashvili, F. Stefani, A. Guseva, and M. Avila, Quasi-two-dimensional nonlinear evolution of helical magnetorotational instability in a magnetized Taylor-Couette flow, New J. Phys. **20**, 013012 (2018).

[37] G. Ogilvie, Instabilities, angular momentum transport, and magnetohydrodynamic turbulence, in *The Solar Tachocline*, edited by D. W. Hughes, R. Rosner, and N. O. Weiss (Cambridge University Press, Cambridge, UK, 2007), p. 299.

[38] Y. Masada, Impact of magnetohydrodynamic turbulence on thermal wind balance in the Sun, Mon. Notices Royal Astron. Soc. Lett. **411**, L26 (2011).

[39] D. Kagan and J. C. Wheeler, The role of the magnetorotational instability in the sun, Astrophys. J. **787**, 21 (2014).

[40] P. A. Gilman, Magnetic buoyancy and magnetorotational instabilities in stellar tachoclines for solar- and antisolar-type differential rotation, Astrophys. J. **867**, 45 (2018).

[41] R. Arlt, A. Sule, and G. Rüdiger, How magnetic is the solar tachocline? in *Proceedings of SOHO 18/GONG 2006/HELAS I, Beyond the Spherical Sun (ESA Special Publication-624)*, edited by K. Fletcher and M. Thompson (CDROM, 2006), p. 74.

[42] A. S. Brun and J. P. Zahn, Magnetic confinement of the solar tachocline, Astron. Astrophys. **457**, 665 (2006).

[43] P. Garaud, Magnetic confinement of the solar tachocline, in *The Solar Tachocline*, edited by D. W. Hughes, R. Rosner, and N. O. Weiss (Cambridge University Press, Cambridge, UK, 2007), p. 147.

[44] R. Arlt, Instabilities in the magnetic tachocline, in *Solar-Stellar Dynamos as Revealed by Helio- and Asteroseismology: GONG 2008/SOHO 21*, edited by M. Dikpati, T. Arentoft, I. González Hernández, C. Lindsey, and F. Hill, ASP Conference Series, Vol. 416 (Astronomical Society of the Pacific, San Francisco, 2009), p. 193.

[45] P. Garaud and J. D. Garaud, Dynamics of the solar tachocline, II. The stratified case, Mon. Notices Royal Astron. Soc. **391**, 1239 (2008).

[46] G. Rüdiger and L. L. Kitchatinov, The slender solar tachocline: A magnetic model, Astron. Nachr. **318**, 273 (1997).

[47] G. Rüdiger and L. L. Kitchatinov, Structure and stability of the magnetic solar tachocline, New. J. Phys. **9**, 302 (2007).

[48] R. Arlt, A. Sule, and R. Filter, Stability of the solar tachocline with magnetic fields, Astron. Nachr. **328**, 1142 (2007).

[49] R. Arlt, A. Sule, and G. Rüdiger, Stability of toroidal magnetic fields in the solar tachocline, Astron. Astrophys. **461**, 295 (2007).

[50] H. M. Antia and S. Basu, Revisiting the solar tachocline: Average properties and temporal variations, Astrophys. J. Lett. **735**, L45 (2011).

[51] L. A. Acevedo-Arreguin, P. Garaud, and T. S. Wood, Dynamics of the solar tachocline, III. Numerical solutions of the Gough and McIntyre model, Mon. Notices Royal Astron. Soc. **434**, 720 (2013).

[52] R. Howe, J. Christensen-Dalsgaard, F. Hill, R. W. Komm, R. M. Larsen, J. Schou, M. J. Thompson, and J. Toomre, Dynamic variations at the base of the solar convection zone, Science **287**, 2456 (2000).

[53] J. P. Zahn, A. S. Brun, and S. Mathis, On magnetic instabilities and dynamo action in stellar radiation zones, Astron. Astrophys. **474**, 145 (2007).

[54] H. C. Spruit, Dynamo action by differential rotation in a stably stratified stellar interior, Astron. Astrophys. **381**, 923 (2002).

[55] T. M. Rogers, Toroidal field reversals and the axisymmetric Tayler instability, Astrophys. J. **735**, 100 (2011).